

# Reciprocal Salt Flux Growth of $\text{LiFePO}_4$ Single Crystals with Controlled Defect Concentrations

Yuri Janssen,<sup>†</sup> Dhamodaran Santhanagopalan,<sup>‡</sup> Danna Qian,<sup>‡</sup> Miaofang Chi,<sup>§</sup> Xiaoping Wang,<sup>||</sup> Christina Hoffmann,<sup>||</sup> Ying Shirley Meng,<sup>‡</sup> and Peter G. Khalifah<sup>\*,†,⊥</sup>

<sup>†</sup>Department of Chemistry, Stony Brook University, Stony Brook, New York 11794, United States

<sup>‡</sup>Department of NanoEngineering, University of California San Diego, La Jolla, California 92093, United States

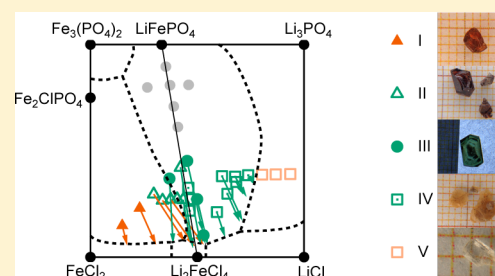
<sup>§</sup>Materials Science and Technology Division and <sup>||</sup>Chemical and Engineering Materials Division, Oak Ridge National Laboratory, Oak Ridge, Tennessee 37831, United States

<sup>⊥</sup>Chemistry Department, Brookhaven National Laboratory, Upton, New York 11973, United States

## S Supporting Information

**ABSTRACT:** Improved methods for the flux growth of single crystals of the important battery material  $\text{LiFePO}_4$  have been developed, allowing the facile preparation of single crystals up to 1 cm across with well-developed facets at relatively low temperatures. The structural characterization of these samples by both powder X-ray diffraction and single crystal diffraction (X-ray and neutron) indicates that the samples are typically stoichiometric with a very low concentration of Fe defects on the Li site, though crystals with larger concentrations of defects can be specifically grown using Fe-rich fluxes. These defects occur through the formation of a Fe-rich  $(\text{Li}_{1-2x}\text{Fe}_x)\text{FePO}_4$  partial solid solution, in contrast to the antisite defects more commonly discussed in the literature which would preserve the ideal  $\text{LiFePO}_4$  stoichiometry. The  $\text{LiFePO}_4$  defects are shown to be sarcopside-like ( $2\text{Li}^+ \rightarrow \text{Fe}^{2+} + \text{vacancy}$ ) based on compositions refined from single crystal diffraction data, the observed dependence of unit cell parameters on defect concentration, and their observed phase behavior (defects only appear in growths from fluxes which are Fe-rich relative to stoichiometric  $\text{LiFePO}_4$ ). The distribution of defects has been studied by aberration corrected scanning transmission electron microscopy and was found to be highly inhomogeneous, suggesting that defect-containing crystals may consist of endotaxial intergrowths of olivine  $\text{LiFePO}_4$  and sarcopside  $\text{Fe}_3(\text{PO}_4)_2$  in a manner that minimizes the detrimental influence of  $\text{Fe}_{\text{Li}}$  defects on the rate of Li-ion transport within crystallites.

**KEYWORDS:** olivine, sarcopside, endotaxy, defects, single crystal, reciprocal salt,  $\text{LiFePO}_4$ ,  $\text{Fe}_3(\text{PO}_4)_2$ ,  $\text{Li}_3\text{PO}_4$ ,  $\text{Fe}_2\text{ClPO}_4$



## 1. INTRODUCTION

Li-ion batteries are an energy storage technology that is playing an increasingly important societal role. In particular, their high energy storage capacity has made Li-ion batteries nearly ubiquitous in high-end portable electronics. Nevertheless, further increases in performance, safety, and cost are necessary before the widespread adoption of this technology in the emerging markets of electric vehicles occurs. A Li-ion cathode material that has been the subject of extensive research and development efforts in the past decade is olivine-type  $\text{LiFePO}_4$ , which has a number of very desirable characteristics including low toxicity, very good thermal stability, and excellent performance at high charge/discharge rates. However, high rate performance  $\text{LiFePO}_4$  typically requires nanostructured powders whose low tap density limits the volumetric capacity of batteries constructed with this cathode material and puts this material at a disadvantage when compared with other materials such as layered  $\text{LiCoO}_2$ -type cathodes that can be incorporated into batteries with larger particle sizes because of their intrinsically higher electronic and ionic conductivities.

Within the olivine structure of  $\text{LiFePO}_4$ , Li ions are arranged in one-dimensional (1D) edge-sharing chains of  $\text{LiO}_6$  octahedra that run parallel to the  $b$ -axis of its  $Pnma$ -symmetry structure. This suggests that Li-ion mobility in  $\text{LiFePO}_4$  is strongly anisotropic and that Li ions will travel along 1D paths when Li is extracted or introduced, a result which is consistent with theory including both phenomenological bond-valence sum maps<sup>1</sup> and quantitative density functional theory (DFT)-based analyses.<sup>2,3</sup> Experimental evidence supporting this diffusion path has been provided by a maximum entropy method (MEM) analysis of neutron diffraction data collected on partially delithiated powder samples at elevated temperatures (620 K), allowing the Li-ion distribution within the unit cell to be visualized.<sup>4</sup>

Although the predicted intrinsic diffusivity along this pathway is believed to be high, ( $D = 10^{-8} \text{ cm}^2/\text{s}$ , ref 2), this fast diffusion channel can be easily blocked because of its low dimensionality,

**Received:** August 16, 2013

**Revised:** October 9, 2013

**Published:** October 10, 2013

and it is not known a priori whether the actual rate of Li diffusion in  $\text{LiFePO}_4$  samples prepared using different methods will be high or low. Theoretical calculations indicate that antisite defects have a low formation energy of 1.13 eV<sup>3,5</sup> that should cause them to form in sufficient quantities to hinder diffusion in samples prepared using common synthesis techniques. Evidence for the presence of Fe ions on the Li site ( $\text{Fe}_{\text{Li}}$  defects) has previously been obtained indirectly through structural refinements of diffraction data for both powder and single-crystal samples of  $\text{LiFePO}_4$ <sup>6,7</sup> and directly from transmission electron microscopy (TEM) studies.<sup>8</sup> When specific models of Li-diffusion motion are studied through DFT- and force-field based methodologies, it is found that antisite defects act as blockades that limit Li-ion diffusion rates,<sup>1,5</sup> forcing diffusing Li ions to move out of the  $\text{LiO}_6$  chains to bypass these blockages.<sup>2</sup> Quantitative modeling showed that both the magnitude and the anisotropy of Li-ion conductivity are strongly influenced by even just 1% of antisite defects.<sup>5</sup> The ionic conductivity in  $\text{LiFePO}_4$  with this level of defects is predicted to decrease by many orders of magnitude, causing the time required for Li to diffuse out of a particle to increase by more than 3 orders of magnitude and with the ionic conductivity becoming far more isotropic.

Single crystals are ideally suited for experimentally resolving the anisotropy of Li-ion conductivity, but very large discrepancies were obtained in two sets of measurements previously published for  $\text{LiFePO}_4$  single crystals. Data collected on crystals grown from the melt using a floating zone technique<sup>9,10</sup> did not find the *b*-axis to have enhanced Li conduction relative to other directions perpendicular to the  $\text{LiO}_6$  chains. However, these results may not reflect the intrinsic properties of  $\text{LiFePO}_4$  since the crystals were found to have Fe ions on about 3% of the Li sites based on the Rietveld refinement of synchrotron powder X-ray diffraction (PXRD) data.<sup>10</sup> In sharp contrast, crystals grown from a LiCl flux<sup>11</sup> were found to have a *b*-axis ionic conductivity more than 2 orders of magnitude higher than the other primary crystallographic axes. Although no values for defect concentrations were reported for the flux-grown crystals, their lower growth temperature should help lower defect concentrations and would suggest that the predictions that antisite defects might obscure the intrinsic anisotropy of the olivine are correct. It is therefore important to obtain quantitative insights into the defect concentrations of flux-grown crystals, especially since  $\text{LiFePO}_4$  with few antisite defects may be expected to have an enhanced Li-ion conductivity that may allow high rate performance with particle sizes large enough to overcome tap density limitations.

Single-crystal samples of  $\text{LiFePO}_4$  have been prepared by a variety of crystal growth methods since the 1930s, and a comparison of these studies suggests that substantial variation in the quality of crystals exists. For example, early hydrothermal techniques<sup>12</sup> produced pink crystals that differed in color from the pale green color commonly reported for powder samples. Later studies on similarly prepared crystals indicated that the pink color may be the result of copper doping.<sup>13</sup> Floating-zone techniques<sup>9,10,14,15</sup> produced a crystal dark enough to appear black rather than green. Although the origin of the black color was not determined, it may be related to the high concentration (~3%) of antisite defects that were reported to form in these samples. Flux growth techniques<sup>11,16–18</sup> have in a number of prior studies been utilized to produce transparent green crystals which, when taken together with the observed fast ion

conduction along the *b*-axis, suggest that these samples are most likely to reflect the intrinsic properties of  $\text{LiFePO}_4$ .

The lowest concentrations of antisite defects are expected to form in crystals grown at intermediate temperatures.  $\text{LiFePO}_4$  crystals grown from the melt (melting point of approximately 1000 °C) should have a relatively high concentration of antisite defects since the entropic stabilization of defects is maximized at this temperature. X-ray diffraction studies on  $\text{LiFePO}_4$  powders annealed at 975 °C (just below its melting point) suggested 4% antisite defects, far more than were originally present after the original solid state synthesis at 685 °C.<sup>6</sup> High defect concentrations can also be induced at overly low growth temperatures where there is insufficient solid state diffusion to anneal out defects. For example, it was shown that hydrothermally produced  $\text{LiFePO}_4$  has about 7% antisite defects as synthesized, but the concentration of these defects can be reduced below the detection limit of PXRD when the samples are annealed at 500 °C,<sup>19</sup> a temperature high enough to permit the solid state diffusion of both Li and Fe ions. Flux grown crystals are therefore expected to be ideal since they can be grown at temperatures hundreds of degrees below that of  $\text{LiFePO}_4$  melts, as judged from the 610 °C melting point of the commonly utilized LiCl flux. Reciprocal salt methods offer a greater degree of control over crystal growth than the use of a single flux, and growth methods using mixed LiCl- $\text{FeCl}_2$  fluxes have been developed in this work as a method for controlling the defect concentration, crystal size, and product yield of  $\text{LiFePO}_4$ .

Single crystal diffraction experiments are unparalleled in the quality of data they produce for structural refinements. Prior high quality  $\text{LiFePO}_4$  single crystal diffraction studies have been published, but only for crystals obtained from hydrothermal methods. The first study of the anisotropic displacement parameters was carried out using hydrothermally grown crystals,<sup>12</sup> and the same type of crystals were also used for charge density studies which used a multipole analysis of the electron density to study the electron distribution along P–O bonds and to gain insights into the Fe 3d orbital occupancies.<sup>20</sup> In contrast, antisite defects in crystals grown by optical floating-zone techniques were studied by the Rietveld refinement of X-ray powder diffraction data,<sup>10</sup> but there has not yet been a published single crystal diffraction study of these samples. Similarly, flux-grown crystals have been used for neutron powder diffraction studies that elucidated the antiferromagnetic structure which appears below 50 K,<sup>16</sup> but single crystal diffraction studies have only been used to confirm the positions of the atoms within the olivine-type structure<sup>18</sup> without examining anisotropic displacement parameters. Time-of-flight neutron powder diffraction has previously been used to study  $\text{LiFePO}_4$  positional parameters and anisotropic displacement parameters,<sup>4</sup> though these studies lack the accuracy and robustness of single crystal diffraction experiments. In this manuscript, the structural analysis  $\text{LiFePO}_4$  crystals has been carried out utilizing flux grown crystals for both single crystal X-ray and single crystal neutron diffraction experiments to obtain precise insights into both the bulk structure and the low concentration defects (<1%) present in olivine single crystal samples grown by reciprocal salt methods. Furthermore, the results have been supplemented by aberration corrected scanning TEM ( $C_s$ -STEM) studies that can directly visualize  $\text{Fe}_{\text{Li}}$  defects. Through these methods, it is demonstrated that flux-grown  $\text{LiFePO}_4$  can be grown either with  $\text{Fe}_{\text{Li}}$  defect concentrations below the detection limit of our SXRD

instrument (0.2%) or with measurable levels of defects (up to 1%), depending on the choice of flux.

## 2. EXPERIMENTAL METHODS

**Crystal Growth.** Single crystals of  $\text{LiFePO}_4$  and byproducts ( $\text{Li}_3\text{PO}_4$  and  $\text{Fe}_2\text{ClPO}_4$ ) were prepared by flux growth techniques.  $\text{Li}_3\text{PO}_4$ ,  $\text{LiCl}$ ,  $\text{FeCl}_2$ , and  $\text{LiFePO}_4$  were used as reagents. When  $\text{LiFePO}_4$  was used, it was prepared from ground mixtures of  $\text{Li}_2\text{CO}_3$ , iron(II) oxalate dihydrate, and diammonium hydrogen phosphate in a  $\text{Li}:\text{Fe}:\text{PO}_4$  molar ratio of 1:1:1 that were heated under flowing  $\text{N}_2$  in open graphite crucibles to temperatures ranging from 950 to 1100 °C. Various molar ratios of reagents were mixed and loaded in loosely covered graphite crucibles. The growth samples were rapidly heated to the highest desired temperature, typically 810 °C, held there for 2 h, and then cooled slowly, typically by 5.5 °C/h, to 480 °C, after which the furnace was allowed to cool naturally. The crucibles were taken out of the furnace, the growth boules were taken out of the crucibles, and the  $\text{LiCl-FeCl}_2$  flux was dissolved with water or ethanol in an ultrasonic bath to reveal the crystals.

**Basic Characterization.** Initially, the crystal growth products were visually inspected, separated by color and form, and weighed. Next the products were characterized by room temperature PXRD using a Bruker D8 Advance diffractometer ( $\text{Cu } K_\alpha$ ,  $\lambda = 1.54059 \text{ \AA}$ ,  $7\text{--}80^\circ 2\theta$ ,  $0.02^\circ$  step size, 300 mm radius, 12 mm variable slits,  $2.5^\circ$  Soller slits, and a 192-channel Lynx-Eye 1D position sensitive Si detector). Scans for phase identification were done at a rate of 0.2 s/step, and scans for lattice parameter determination were done at 0.8 s/step. Zero background Si slides were used as sample holders. Phase identification was performed using the software package JADE v9.1.1 (Materials Data, Inc.). Accurate lattice parameters for  $\text{LiFePO}_4$  were determined with the Le Bail method as implemented in the computer program JANA2006.<sup>21</sup>

**Single Crystal Diffraction.** Single crystal experiments were done using both X-ray and neutron diffraction. X-ray diffraction data were collected at room temperature with an Oxford Diffraction Gemini Atlas diffractometer using  $\text{Mo } K_\alpha$  radiation. Data reduction and analytical face-indexed absorption corrections using the measured crystal shape were performed using CrysAlisPro (171.35.19). The crystal structures were refined using the program Jana2006.<sup>21</sup> In addition, face-indexed crystal shape models were determined from crystals, up to 2 mm in maximum dimension using a Bruker Kappa Apex II X-ray diffractometer. Room-temperature neutron diffraction data were measured on the instrument TOPAZ at the Spallation Neutron Source (SNS) at Oak Ridge National Laboratory, in the wavelength-resolved time-of-flight Laue diffraction mode using neutron wavelengths in the range of 0.5 to 3.2 Å. A crystal of  $1.9 \times 1.9 \times 2.5 \text{ mm}^3$  was selected from a batch for which a smaller crystal was also studied in single crystal X-ray diffraction experiments. The data were unaffected by magnetic order, whose onset temperature is around 50 K. The linear absorption length of  $\text{LiFePO}_4$  at  $\lambda = 1.8 \text{ \AA}$  is calculated to be  $1.0 \text{ cm}^{-1}$ . Data reduction and spherical absorption corrections were made using the local ANVRED2 program in ISAW. Structural refinements were done in the program GSAS, which can handle wavelength-dependent extinction effects.<sup>22</sup>

**Sample Cutting.** Face-indexed  $\text{LiFePO}_4$  single crystals were oriented and fixed on a scanning electron microscopy (SEM) stub to enable focused ion beam (FIB) lift out from a (100) facet of the crystal, as shown in Supporting Information, Figure S1. Two micrometers of Pt were deposited in the FIB on the (100) facet of the crystal prior to lift out. Typical dimensions of the cut slab are  $6 \times 2 \times 20 \text{ }\mu\text{m}^3$  and a standard lift out procedure was followed using an Omni-probe. The resulting  $\text{LiFePO}_4$  slab was mounted on a commercial copper grid for TEM. The slab was thinned down to a thickness of about 70 nm to allow imaging parallel to the crystal *b*-axis. The side and top view of the thin portion of the crystal used for imaging are also shown in Supporting Information, Figure S1. Prior to imaging, the surface amorphous layer was removed by low energy  $\text{Ar}^+$  milling (3 keV, 3 mA for 10 min).

**Imaging of Defects.** TEM/STEM studies were carried out on a Cs-corrected FEI Titan 80/300-kV TEM/STEM microscope equipped with a Gatan Image Filter Quantum-865. Scanning TEM (STEM) images were acquired at 300 kV and with a beam size of  $\sim 0.7 \text{ \AA}$ . High-angle annular dark field (HAADF) images (also called *Z*-contrast images since the contrast is proportional to atomic number, varying as  $Z^{1.7}$ ) were obtained with a convergence angle of 30 mrad and a large inner collection angle of 65 mrad. This contrast was used to visualize the lithium columns that contain iron ions with much higher *Z*. To minimize possible electron beam irradiation effects, HAADF figures presented in this work were acquired from areas without prior beam irradiation.

## 3. RESULTS AND DISCUSSION

### Reciprocal Salt Flux Growth of $\text{LiFePO}_4$ : Expectations.

Mixed  $\text{LiCl-FeCl}_2$  fluxes can be used to gain an unprecedented degree of control over the growth of  $\text{LiFePO}_4$  crystals in a manner best understood through a phase diagram of reciprocal salts. The use of a flux when growing  $\text{LiFePO}_4$  crystals offers a number of advantages over the solidification of  $\text{LiFePO}_4$  melts. Crystals can be grown at temperatures which are substantially lower as a result of the eutectics that form in multicomponent melts. This is expected to offer both cost advantages (relevant for industrial processes) and crystal quality advantages (low growth temperatures will minimize entropically stabilized defects; slower growth rates may enhance crystal perfection). The quality of flux-grown crystals is reflected in the fast *b*-axis ionic conductivity reported previously. Many fluxes, such as the  $\text{LiCl}$  used in prior preparations of  $\text{LiFePO}_4$  crystals, have a high solubility in water and can easily be removed after the growth allowing the isolation of large  $\text{LiFePO}_4$  product crystals (few millimeters in size).

Although  $\text{FeCl}_2$  has been used as a starting reagent, it has not previously been explored as a flux for the growth of olivine crystals since previous studies on the flux growth of  $\text{LiFePO}_4$  and other olivine  $\text{LiMPO}_4$  compounds ( $M = \text{Fe, Mn, Co, Ni}$ ) have been confined to compositions that fall directly on the  $\text{LiMPO}_4\text{--LiCl}$  compositional line, labeled C in Figure 1. For example, the flux growth of  $\text{LiFePO}_4$  has traditionally been accomplished by melting an equimolar mixture of  $\text{LiCl}$ ,  $\text{FeCl}_2$ , and  $\text{Li}_3\text{PO}_4$ , which after melting may be considered to behave as a mixture of  $\text{LiFePO}_4$  and  $\text{LiCl}$  in a 1:3 molar ratio.<sup>16–18,23</sup> When we revisited the  $\text{LiFePO}_4\text{--LiCl}$  compositional line (samples were prepared by mixing presynthesized  $\text{LiFePO}_4$  with a  $\text{LiCl}$  salt), the products of growths were a mixture of  $\text{LiFePO}_4$  and  $\text{Li}_3\text{PO}_4$  crystals, indicating that  $\text{LiFePO}_4$  and  $\text{LiCl}$  do not form a simple eutectic system. Similarly, a mixture of  $\text{LiFePO}_4$  and a flux rich in  $\text{FeCl}_2$  also produced crystals of a third phase,  $\text{Fe}_2\text{ClPO}_4$ , indicating that  $\text{FeCl}_2$  by itself is also not an ideal for growing  $\text{LiFePO}_4$  either. The phase behavior of these two fluxes that leads to the production of undesired secondary phases is schematically illustrated in Figure 1, panels A and C, with an expanded discussion of the construction of this phase diagram provided in the Supporting Information (Figure S2).

The use of  $\text{LiCl-FeCl}_2$  mixtures allows an additional dimension of phase space to be accessed, and lead to the discovery that a simple pseudobinary eutectic growth of  $\text{LiFePO}_4$  can be achieved using mixed  $\text{LiCl-FeCl}_2$  fluxes. An example of this is illustrated for the  $\text{LiFePO}_4\text{--Li}_2\text{FeCl}_4$  system for which an estimated approximate representation is given in Figure 1, panel B. When a melt of these substances mixed in a 1:3 ratio (on the scale of the graph) is cooled, crystal nucleation and solidification will begin at about 700 °C when the liquidus

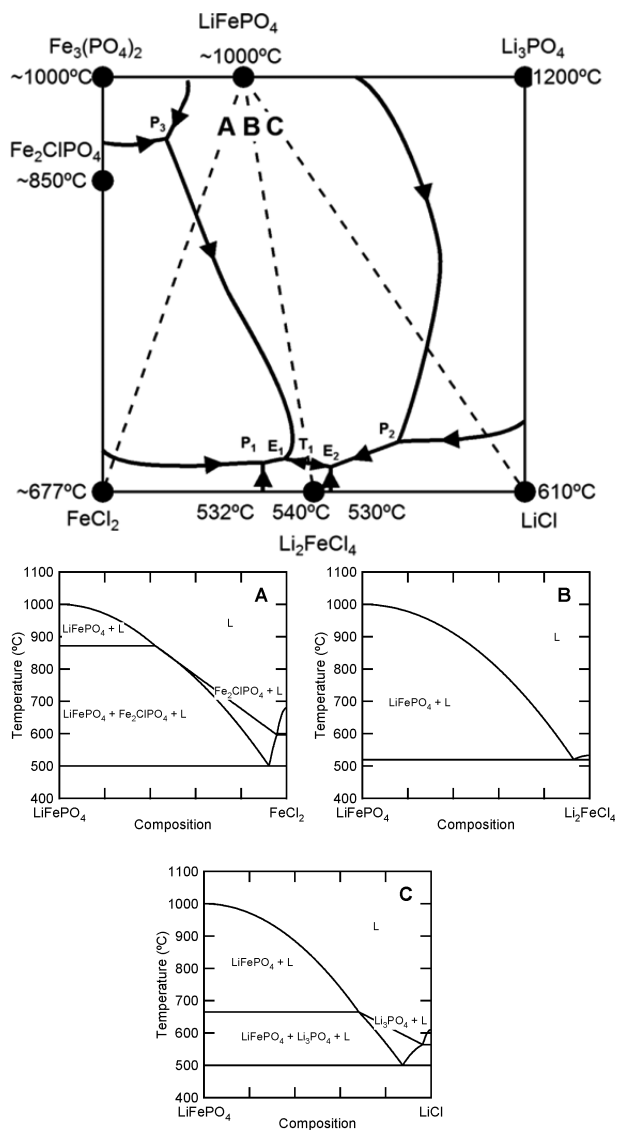


**Figure 1.** Estimated phase diagram for in the  $\text{Li,Fe,Cl,PO}_4$  reciprocal salt system, with melting points of stable phases indicated. The horizontal axis is the charge fraction from Li,  $[\text{Li}]/([\text{Li}]+2[\text{Fe}])$ , while the vertical axis is the charge fraction from  $\text{PO}_4$ ,  $3[\text{PO}_4]/(3[\text{PO}_4]+[\text{Cl}])$ . The cuts along joins A, B, and C are shown below with similarly scaled axes. Join B (to  $\text{Li}_2\text{FeCl}_4$ ) is a true binary join, unlike joins A ( $\text{FeCl}_2$ ) and C ( $\text{LiCl}$ ) for which other phases also form during solidification.

line is reached. As the melt is further cooled, the crystal will grow, causing the liquid to become gradually depleted of  $\text{LiFePO}_4$  and causing the system composition to evolve along the path of the liquidus line. Finally, at the eutectic temperature of about  $520^\circ\text{C}$ , the liquid freezes to form a mixture of microcrystalline  $\text{LiFePO}_4$  powder and solid  $\text{Li}_2\text{FeCl}_4$  flux, which will coexist in the final product with the large  $\text{LiFePO}_4$  crystals that previously formed. Increasing the concentration of  $\text{LiFePO}_4$  in the melt will result in a larger mass of single crystal  $\text{LiFePO}_4$  being produced, while increasing the concentration of flux will reduce the temperatures at which  $\text{LiFePO}_4$  crystals are grown up until the composition of the eutectic is reached. Beyond that point, the crystal growth of  $\text{Li}_2\text{FeCl}_4$ , rather than  $\text{LiFePO}_4$  will be promoted by cooling. Although precise details of the  $\text{LiFePO}_4$ – $\text{Li}_2\text{FeCl}_4$  system have not been determined experimentally, it is known that  $\text{Li}_2\text{FeCl}_4$

has a melting point of  $540^\circ\text{C}$ ,<sup>24</sup> which is about  $450^\circ\text{C}$  lower than that of  $\text{LiFePO}_4$ , and which will result in a eutectic temperature that likely is a little below  $540^\circ\text{C}$ , and which was subjectively estimated to be  $520^\circ\text{C}$  for this diagram. Although the  $\text{LiFePO}_4$ – $\text{Li}_2\text{FeCl}_4$  eutectic composition is unknown, it can be inferred by isolating and weighing the large single crystal(s) produced during the growth, and its position was estimated based on the results of multiple single crystal growth experiments with flux compositions at or near  $\text{Li}_2\text{FeCl}_4$ —a procedure that was used to gain an understanding of the generalized phase diagram relevant to the crystal growth of  $\text{LiFePO}_4$ .

There are at most two different anions and two different cations in any mixture of  $\text{LiFePO}_4$  and the two fluxes of interest ( $\text{LiCl}$  and  $\text{FeCl}_2$ ), namely,  $\text{Li}^+$ ,  $\text{Fe}^{2+}$ ,  $\text{Cl}^-$ , and  $\text{PO}_4^{3-}$ . These four ions can therefore be used to construct the  $\text{Li,Fe,Cl,PO}_4$  reciprocal salt system, which can be utilized to efficiently represent this system as a phase diagram, allowing us to comprehensively understand the growth pathways for  $\text{LiFePO}_4$  single crystals using mixed  $\text{LiCl}$  and  $\text{FeCl}_2$  fluxes. This reciprocal salt system is constructed from two cations ( $\text{Li}^+$  and  $\text{Fe}^{2+}$ ) and two anions ( $\text{Cl}^-$  and  $\text{PO}_4^{3-}$ ) and is arranged in a square where the corner compositions are composed by the pairing of respectively one type of cation and one type of anion (Figure 1). The presence and position of important elements in the phase diagram (primary solidification boundaries, eutectics, etc.) are influenced by the stable crystalline phases that exist within its boundaries. In this system, the four corners of the phase diagram consist of the known phases  $\text{Fe}_3(\text{PO}_4)_2$ ,  $\text{Li}_3\text{PO}_4$ ,  $\text{LiCl}$ , and  $\text{FeCl}_2$  which are marked by solid circles in Figure 1. Three additional phases combining three-component ions are known to be thermodynamically stable above  $300^\circ\text{C}$ , namely,  $\text{LiFePO}_4$ ,  $\text{Fe}_2\text{PO}_4\text{Cl}$ , and  $\text{Li}_2\text{FeCl}_4$ . The seven compounds known for this system are all congruently melting, making each of them part of their own primary solidification surface, and which will ensure the presence of a eutectic point for each pair of neighboring compounds. Since the primary solidification field of  $\text{LiFePO}_4$  represents the region in which only this phase will nucleate and grow as the liquid is cooled below its melting point, this region in the center of the phase diagram is of greatest interest for the present study. Regardless of the initial melt composition for  $\text{LiFePO}_4$  crystal growth in this region, the liquid composition will evolve in a straight line away from the circle marking the composition of  $\text{LiFePO}_4$  as this is the composition of solid which is removed from the liquid during crystallization. No four-component phases are known. An eighth ternary phase,  $\text{Li}_6\text{FeCl}_8$ , that falls within the boundaries was neglected since it is only stable below  $250^\circ\text{C}$ <sup>24</sup> and can therefore not be accessed through any melt in this reciprocal salt system. Further details about this approach are provided in the Supporting Information.

The full mapping of the solidification pathways and temperatures within this reciprocal salt diagram is an exhaustive process for which shortcuts were utilized to enable us to reach our specific goals of (1) producing large crystals with low defect concentrations suitable for studying the intrinsic structural, physical, and electrochemical properties of  $\text{LiFePO}_4$ , (2) identifying starting compositions which can be used to produce high quality crystals of  $\text{LiFePO}_4$  at low temperatures using easily removed salts without the concomitant production of macroscopic crystals of insoluble phases like  $\text{Li}_3\text{PO}_4$ , and (3) identifying starting compositions useful for producing high-quality  $\text{LiFePO}_4$  in high yield with minimal usage of flux. A

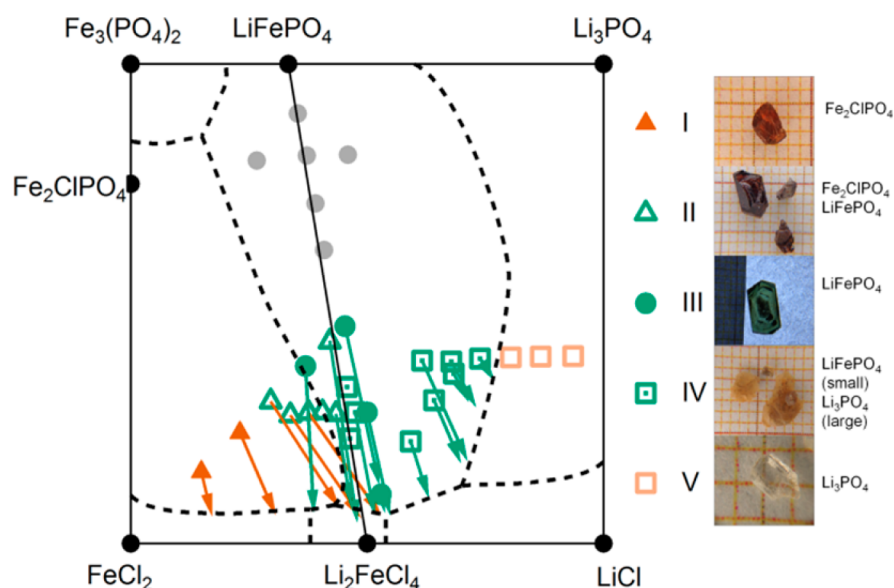


**Figure 2.** Reciprocal salt square for the system  $\text{Li,Fe,Cl,PO}_4$ , relevant for the flux growth of  $\text{LiFePO}_4$ . Each of the five types of growth products (I–V) are marked with a different symbol, as shown in the legend on the right along with a picture of representative products. Arrows indicate the evolution of composition during growth for the phase whose crystals were weighed (red for  $\text{Fe}_2\text{ClPO}_4$ , green for  $\text{LiFePO}_4$ ). Dashed lines indicate the estimated primary solidification boundaries for these phases, parts of which could be accurately estimated from mass changes.

series of trial growths were therefore carried out at compositions within this reciprocal salt system. Based on an evaluation of the phases that grew as large single crystals and aided by the quantification of the masses of  $\text{LiFePO}_4$  growth products, a good understanding of available growth pathways for meeting these goals was achieved with minimal effort. These results are summarized in Figure 2, and are discussed in more detail below.

#### Reciprocal Salt Flux Growth of $\text{LiFePO}_4$ : Experiment.

The first step to exploring the  $\text{Li,Fe,Cl,PO}_4$  reciprocal salt system was to identify a satisfactory crucible material, as the sealed pinhole platinum crucibles used previously are not conducive to exploratory growths over a wide range of compositions. Alternative crucible choices were tried, and alumina proved unsatisfactory because of reactivity with the flux. Iron crucibles successfully contained the flux, but they yielded smaller crystals than the inexpensive graphite crucibles that were determined to be optimal. Graphite does not contribute chemical contaminants since carbon cannot substitute for any of the  $\text{LiFePO}_4$  constituent elements, and it naturally provides an actively reducing environment suitable for keeping iron in its reduced divalent state. Furthermore, the ease of separation and observed contact angle of the product boules suggested that the flux did not wet the crucible, an observation consistent with the small number of large  $\text{LiFePO}_4$  crystals nucleated during the growth. Sometimes only a single nucleation event occurred, resulting in the growth of one single crystal up to one centimeter in width and one gram in mass. Olivine crystals were typically greater than one millimeter in their maximum dimension and could therefore be trivially isolated from the flux or from competing phases that also grew as single crystals.

Pictures of the most common types of single crystal growth products and the regions in phase space where they formed are shown in Figure 2. After dissolution of the chloride flux and other soluble components in water/ethanol, the three primary phases observed as growth products were  $\text{LiFePO}_4$ ,  $\text{Li}_3\text{PO}_4$ , and  $\text{Fe}_2\text{ClPO}_4$ . Neither  $\text{Fe}_3(\text{PO}_4)_2$  nor any new phases were found

in these experiments, which did not include a full survey of all possible starting compositions. Sometimes, a small weight percentage of magnetite ( $\text{Fe}_3\text{O}_4$ ) was found. This is believed to reflect an impurity associated with oxidation, but did not seem to have a large influence on the growth products nor on their amounts.  $\text{LiFePO}_4$ ,  $\text{Li}_3\text{PO}_4$ , and  $\text{Fe}_2\text{ClPO}_4$  were either found as millimeter-sized faceted crystals or as microcrystalline powders, with their morphology providing information about their growth mechanism. Large crystals result from either primary solidification or from cosolidification, and microcrystalline powders result from rapid solidification at or near the eutectic where freezing of the melt occurred. The  $\text{LiFePO}_4$  crystals obtained for the present paper had well-defined facets organized into a prismatic equant growth habit with up to 14 major facets, as seen in Supporting Information, Figure S3. The major facets of the  $\text{LiFePO}_4$  crystals belonged to the same four classes of  $\{100\}$ ,  $\{101\}$ ,  $\{210\}$ , and  $\{011\}$  that were observed in growths from a pure  $\text{LiCl}$  flux.<sup>23,25</sup> These facets do not agree with the Wulff shapes calculated using DFT,<sup>26</sup> a method which usually does not take into account interactions between the growing crystal and the salt flux, and also differ from those observed in hydrothermal growths.<sup>7,27</sup>

Further insights into the growth processes could be inferred from the masses of the large single crystal products of  $\text{LiFePO}_4$ ,  $\text{Li}_3\text{PO}_4$ , and  $\text{Fe}_2\text{ClPO}_4$ , which could be simply identified by color and which could be easily separated when they coexisted because of their size. Weighing the large crystals and subtracting their mass from the starting composition (shown as vectors in Figure 2) allowed the eutectic composition to be inferred and enabled the construction of a partial phase diagram with the approximate solidification boundaries. Consistent growth products were obtained based on composition, and five different regions (I–V) were identified. When found as the only large crystals,  $\text{Fe}_2\text{ClPO}_4$  (I) appeared as transparent red prismatic crystals (0.5–5 mm),  $\text{LiFePO}_4$  crystals (III) were transparent green prismatic crystals (0.5–5 mm), and  $\text{Li}_3\text{PO}_4$  (V) appeared as transparent colorless prismatic crystals (0.5–1 mm).  $\text{Fe}_2\text{ClPO}_4$  was found to be hydrophilic, and hydrated

over a time period of a few hours when exposed to air. Sometimes larger crystals of different types were found together. In region II, crystals of  $\text{LiFePO}_4$  were found both attached to and intergrown with  $\text{Fe}_2\text{ClPO}_4$  crystals. Such intergrown crystals are still hydrophilic, and fall apart when exposed to air for days or weeks. Crystals of  $\text{LiFePO}_4$  were also found together with crystals of  $\text{Li}_3\text{PO}_4$  (IV), which then appeared as opaque pink crystals (0.5–3 mm), consistent with prior reports.<sup>23</sup>

**Defect Concentrations in  $\text{LiFePO}_4$  Crystals.** Since defects are expected to strongly influence the behavior of  $\text{LiFePO}_4$  as a cathode material, diffraction experiments were carried out to quantify the bulk defect concentration of single crystals prepared by the flux growth methods discussed above. Defects can be probed both indirectly (through their influence on lattice parameters) and directly (through refinements of site occupancies) in diffraction studies. A number of prior studies have found that defects increase the unit cell volume of  $\text{LiFePO}_4$ .<sup>6,7,19,28</sup> The most sensitive method for determining lattice parameters is PXRD, which has the advantages (over single crystal diffraction studies) of a fixed diffractometer geometry and a large sample-to-detector distance, though lattice parameters refined on different instruments or using different software algorithms are not necessary directly comparable. Reported values for the unit cell volume of  $\text{LiFePO}_4$  synthesized by solid state methods range from 290.99  $\text{\AA}^3$  (ref 28) to 291.25  $\text{\AA}^3$  (ref 6), whereas hydrothermally produced but high temperature annealed  $\text{LiFePO}_4$  was reported to have a somewhat larger volume of 291.66  $\text{\AA}^3$  (ref 7). The refinement of atomic site occupancies using high quality single crystal X-ray diffraction (SXRD) data can more directly probe the presence of defects, though the sensitivity of this method varies greatly with the ion being probed. It is difficult to distinguish between Li ions and vacancies which have low and zero scattering factors, respectively. In contrast, the method has good sensitivity to the presence of Fe on Li sites ( $\text{Fe}_{\text{Li}}$ ) and to any defect on the Fe site ( $\text{Li}_{\text{Fe}}$  or vacancy) because of the contrast provided by the much larger scattering factor of Fe.

To characterize the defect concentration in  $\text{LiFePO}_4$  crystals grown using reciprocal flux methods, PXRD experiments were carried out on ground crystals prepared from eight different flux starting compositions, and SXRD experiments were carried out on one additional crystal from each batch. The compositions of all nine batches within the overall phase diagram are marked in Figure 3, with the experimentally determined cell volumes and defect compositions plotted directly below. The samples for PXRD were two to four  $\text{LiFePO}_4$  single crystals ground together, with a Le Bail refinement used to fit their lattice parameters. The range of observed unit cell volumes substantially exceeded the experimental precision, suggesting that not all  $\text{LiFePO}_4$  crystals growths result in the same final composition. The three crystal growths with the most Fe-rich compositions (starting compositions to the left of the tie line between  $\text{LiFePO}_4$  and  $\text{Li}_2\text{FeCl}_4$ ) had the largest cell volumes, with the volume increasing with the initial Fe content. SXRD experiments on the three crystals from these growths found that all three had excess scattering power on the Li site, indicating the presence of  $\text{Fe}_{\text{Li}}$  defects as will be discussed in more detail later. This behavior is consistent with prior reports of the formation of a  $\text{Li}_{1-2x}\text{Fe}_{1+x}\text{PO}_4$  solid solution in which  $\text{LiFePO}_4$  can have sarcopside-like defects,<sup>7,19,28–30</sup> but for the first time the evolution in unit cell volume (from PXRD) can be directly correlated with a direct measurement of the defect type

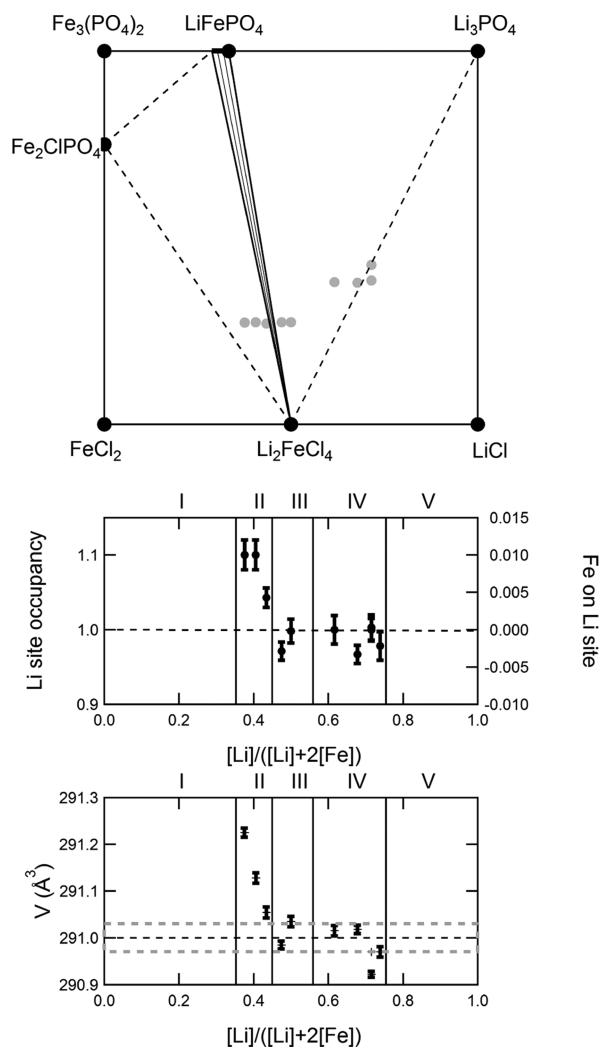


**Figure 3.** Top:  $\text{Li,Fe,Cl,PO}_4$  reciprocal salt diagram including initial growth compositions (gray) of eight crystal growth batches used for structural characterization with both PXRD and SXRD experiments. The tie line between  $\text{Li}_2\text{FeCl}_4$  and  $\text{LiFePO}_4$  is marked, and is broadened to indicate a limited sarcopside-type  $\text{Li}_{1-2x}\text{Fe}_{1+x}\text{PO}_4$  solid solution on the Fe-rich side. Dotted lines are a tentative triangulation of the system into a phase diagram under sample growth conditions (500–800 °C, reducing atmosphere). Middle: Freely refined Li site occupancies (left axis) and corresponding concentration of  $\text{Fe}_{\text{Li}}$  defects (right axis) for crystals grown from flux compositions marked in the top panel. Bottom: Unit cell volume determined by PXRD for the same crystal growth batches.

and concentration (from SXRD) in samples whose anisotropic properties (such as electronic and ionic conductivity) can be measured using complementary techniques such as impedance spectroscopy. Flux compositions that were Fe-rich relative to the ideal 1:1 Li:Fe ratio of  $\text{LiFePO}_4$  resulted in the incorporation of excess Fe into samples during growth, though in contrast to solid state reactions the composition of the crystal products does not need to preserve the starting Li:Fe ratio because of potential differences in activity of the ions dissolved in the flux. The reciprocal salt method can therefore be used to prepare single crystals with variable defect concentrations enabling the influence of defects on  $\text{LiFePO}_4$  properties to be studied.

Alternatively,  $\text{LiFePO}_4$  crystals with extremely low defect concentrations could be reproducibly grown from reciprocal

salt fluxes whose starting compositions were on the Li-rich side of the tie line between  $\text{LiFePO}_4$  and  $\text{Li}_2\text{FeCl}_4$ . This portion of the phase diagram closely corresponds to regions III and IV in the phase diagram that either produced large crystals of only  $\text{LiFePO}_4$  or of both  $\text{LiFePO}_4$  and  $\text{Li}_3\text{PO}_4$ . Examination of the unit cell lattice parameters and volume (which were all within 2 standard deviations of the average value) as well as a wider range of crystallographic parameters (Supporting Information, Figure S7) suggests that the remaining six starting compositions for growth result in indistinguishable products under our standard growth protocol (crystal growths in graphite crucibles that are cooled from 810 to 500 °C under flowing  $\text{N}_2$ ). The average lattice parameters of these six samples are  $a = 10.3298(5)$  Å,  $b = 6.0062(3)$  Å, and  $c = 4.6902(4)$  Å with a unit-cell volume of  $V = 290.99(4)$  Å<sup>3</sup>, where these esds now represent scatter between refined values rather than the accuracy of any one single refinement.

The full crystallographic refinement of these samples suggests that the concentration of site defects is low relative to the measurement uncertainty of about 0.2% on both the Fe and the Li sites, as will be discussed in detail in the next section. Based on the observed phase behavior mapped during the investigation of reciprocal salt flux growths, it can be concluded that prior  $\text{LiFePO}_4$  single crystal growths using  $\text{LiCl}$  as a flux<sup>11</sup> also resulted in the production of crystals with very low defect concentrations despite the fact that these crystals were not fully characterized structurally, if neither the flux nor the crucible introduced external impurities. It should be noted that the use of mixed  $\text{LiCl-FeCl}_2$  reciprocal salt fluxes is more advantageous for industrial preparations since they can produce low defect concentration  $\text{LiFePO}_4$  crystals without accompanying  $\text{Li}_3\text{PO}_4$  crystals that need to be separated before growth products can be incorporated into batteries.

Single crystal X-ray diffraction investigations into the crystal structure of  $\text{LiFePO}_4$  were carried out through the refinement of room temperature data collected on 11 different crystals obtained from 9 different growth batches, using crystals with sizes ranging from 0.0034 to 0.057 mm<sup>3</sup> (mean thickness of 0.15–0.4 mm). The studied crystals had well-defined facets which facilitated an analytical face-indexed absorption correction using crystal dimensions measured from a set of calibrated video images. Further details of the experimental parameters are given in Supporting Information, Table S2. The resulting data sets were first refined against the literature structure of  $\text{LiFePO}_4$  without allowing disorder, and all crystallographic parameters were in good agreement with those reported previously.<sup>12,20</sup> Moreover, the refined parameters for low-disorder samples (4–10) were in agreement, as none of the refined crystallographic parameters was more than three standard deviations from the mean across samples (Supporting Information, Figure S7), suggesting that the intrinsic properties of  $\text{LiFePO}_4$  can be readily accessed when the proper corrections for extinction and absorption are applied. Refined fractional coordinates for one of the crystals from the batch that was also used in the neutron experiment (X9) are given in Table 1, while anisotropic displacement parameters (ADPs, shown in Supporting Information, Figure S4) and selected bond lengths and angles are given in Table 2, and Supporting Information, Tables S3, and S4, respectively. The present  $\text{LiFePO}_4$  atomic coordinates are in general agreement with prior single crystal refinement studies,<sup>12,20</sup> though larger differences are observed in the anisotropic displacement parameters (ADPs). It should be noted that Yakubovich et

**Table 1. Comparison of Atomic Site Positions and Isotropic Displacement Parameters ( $U_{\text{eq}}$ ) Refined from X-ray (in bold) and Neutron Diffraction Data**

site	<i>x</i>	<i>y</i>	<i>z</i>	$U_{\text{eq}}$ (Å <sup>2</sup> )
Li	<b>0</b>	<b>0</b>	<b>0</b>	<b>0.0169(5)</b>
Li	0	0	0	0.0171(6)
Fe	<b>0.282211(11)</b>	1/4	<b>0.97472(3)</b>	<b>0.00672(3)</b>
Fe	0.28218(4)	1/4	0.97465(8)	0.00598(7)
P	<b>0.094859(19)</b>	1/4	<b>0.41827(4)</b>	<b>0.00538(4)</b>
P	0.09478(6)	1/4	0.41869(13)	0.00494(11)
O1	<b>0.09697(6)</b>	1/4	<b>0.74260(12)</b>	<b>0.00840(12)</b>
O1	0.09706(7)	1/4	0.74240(13)	0.00792(11)
O2	<b>0.45720(6)</b>	1/4	<b>0.20584(13)</b>	<b>0.00813(12)</b>
O2	0.45717(7)	1/4	0.20580(13)	0.00791(11)
O3	<b>0.16557(4)</b>	<b>0.04656(7)</b>	<b>0.28492(9)</b>	<b>0.00837(8)</b>
O3	0.16557(5)	0.04653(8)	0.28462(9)	0.00810(9)

al.<sup>12</sup> did not correct their data for absorption and extinction, whereas Streltsov et al. did correct for absorption and extinction, but did not report ADPs.

The availability of large single crystals of olivine  $\text{LiFePO}_4$  enables single crystal neutron diffraction (SND) studies which typically have enhanced sensitivity to light elements (relative to SXRD studies) because of two factors. The first is the decoupling of scattering power from atomic number. The neutron scattering lengths for Fe (9.45 fm), P (5.13 fm), and O (5.81 fm) are substantial, though it should be noted that Li (−1.9 fm) still remains the atom to which the diffraction experiment is least sensitive. Second, neutrons are sensitive to the nucleus rather than the electron cloud and will not experience the drop-off in diffraction peak intensity at shorter *d*-spacings inherent to X-ray form factors nor the artifacts caused by bonding-induced spatial redistributions of valence electrons that cause deviations from the standard spherical atom models routinely used in refinements of X-ray diffraction data. Time-of-flight neutron diffraction data on one single crystal was therefore carried out on the newly commissioned TOPAZ single crystal diffractometer at the Spallation Neutron Source (SNS) at Oak Ridge National laboratory, which has substantial advantages in flux and resolution over single crystal diffractometers located at other neutron sources.<sup>31</sup> A spherical absorption correction with a wavelength-dependent absorption coefficient was applied. Extinction corrections were also essential, as the crystals had an unusually high degree of perfection comparable to those of crystals used for synchrotron monochromators. Further experimental details are described in the Supporting Information, and are summarized in Supporting Information, Tables S5. Refined fractional coordinates are given in Table 1, anisotropic displacement parameters (ADPs) in Table 2, and selected bond lengths and angles in Supporting Information, Tables S6 and S7.

The fractional coordinates and displacement parameters obtained independently by X-ray diffraction and by neutron diffraction, respectively, are in excellent agreement, as seen in Tables 1 and 2. All atom coordinates agree within 0.005 Å, and the equivalent isotropic displacement parameters  $U_{\text{eq}}$  are within 1–5% of each other, except for Fe, for which the neutron diffraction results are about 10% smaller than the X-ray results. When the anisotropic displacement parameters are compared, very good agreement is again seen in each of their six separate components. It is expected that even better agreement in the APDs may be possible in the future if a face-indexed absorption

Table 2. Comparison of Anisotropic Displacement Parameters from X-ray (in bold) and Neutron Data

site	$U_{11}$ (Å <sup>2</sup> )	$U_{22}$ (Å <sup>2</sup> )	$U_{33}$ (Å <sup>2</sup> )	$U_{12}$ (Å <sup>2</sup> )	$U_{13}$ (Å <sup>2</sup> )	$U_{23}$ (Å <sup>2</sup> )
Li	<b>0.0212(10)</b>	<b>0.0157(9)</b>	<b>0.0138(8)</b>	−0.0029(7)	−0.0019(6)	−0.0038(6)
Li	0.0193(11)	0.0151(9)	0.0170(9)	−0.0021(9)	−0.0010(7)	−0.0035(8)
Fe	<b>0.00648(5)</b>	<b>0.00599(5)</b>	<b>0.00769(5)</b>	0	<b>0.00037(3)</b>	0
Fe	0.00549(12)	0.00558(12)	0.00686(11)	0	0.00030(7)	0
P	<b>0.00567(8)</b>	<b>0.00567(7)</b>	<b>0.00479(7)</b>	0	<b>0.00020(5)</b>	0
P	0.00468(20)	0.00586(18)	0.00429(17)	0	0.00022(12)	0
O1	<b>0.0097(2)</b>	<b>0.0104(2)</b>	<b>0.00511(18)</b>	0	−0.00012(15)	0
O1	0.00893(22)	0.01033(22)	0.00450(17)	0	−0.00033(12)	0
O2	<b>0.0058(2)</b>	<b>0.0105(2)</b>	<b>0.00806(19)</b>	0	<b>0.00035(15)</b>	0
O2	0.00551(19)	0.01096(23)	0.00726(17)	0	0.00031(11)	0
O3	<b>0.01034(16)</b>	<b>0.00676(14)</b>	<b>0.00802(14)</b>	<b>0.00236(11)</b>	<b>0.00142(11)</b>	<b>0.00021(11)</b>
O3	0.00967(18)	0.00695(15)	0.00766(13)	0.00243(12)	0.00102(9)	0.00018(11)

correction can be utilized for the neutron data, or if less absorbing isotopic<sup>7</sup> Li crystals are studied. The agreement between the structural parameters measured by X-ray and neutron diffraction, two very different techniques with different corrections and systematic errors, indicates that they both are accurate and have sufficient sensitivity to accurately model the behavior of both heavy and light atoms. Given the large masses of crystals that can be readily produced in a single growth batch, powders prepared by grinding these crystals could serve as a standard for displacement parameters suitable for any type of diffractometer (such as X-ray or time-of-flight neutron powder diffractometers with 2D detectors) to ensure that instrumental parameters do not interfere with the accurate determination of displacement parameters. Since displacement parameters correlate with site occupancies, it is important to have great confidence in an instrumental model when trying to use Rietveld refinement of powder diffraction data to make judgments about the occupancies of sites that are mixed or contain vacancies. Furthermore, these accurately determined LiFePO<sub>4</sub> displacement parameters may be used as fixed input or constraints in refinements of doped or defective LiFePO<sub>4</sub> structures studied by powder diffraction techniques to eliminate correlations when refining site occupancies, avoiding a major source of systematic errors and leading to more accurate insights into site occupancies.

After ensuring that the raw data were processed in an optimal manner, the single crystal diffraction data were analyzed to determine whether small quantities (~1%) of defects within the olivine structure could be directly resolved using these high quality data sets. By refining site occupancies, estimates could be made for the detection limit of defects as well as for the likely defect concentration within these flux-grown crystals of LiFePO<sub>4</sub>. Surprisingly, the limiting sources of errors in determining occupancies came not from the data quality but from the conventional atomic form factors which are nearly universally used for the structural refinement of single crystal diffraction data. It is apparent that covalent bonding effects are sufficiently strong to influence the interpretation of single crystal diffraction data, and could potentially be used to carry out comparative studies of the inductive effect among different oxoanion battery materials (an analysis that is beyond the scope of this work). The final analysis of Li and Fe site occupancies (Row 4, Supporting Information, Table S8) was therefore carried out with the P occupancy fixed at 1 but with the oxygen occupancies allowed to refine to aphysical values slightly greater than 1 to minimize systematic errors at the Li and Fe positions caused by correlations (likely mediated through the overall

refinement scale factor) with improperly modeled electron density for oxygen atoms, with the justification of this approach given in the Supporting Information. The final results are concisely summarized in Table 3.

Table 3. Refined Occupancies of Li and Fe Sites in LiFePO<sub>4</sub><sup>a</sup>

sample	melt	Li	Fe
X1 <sup>b</sup>	0.375	1.100(20)	1.000(2)
X2 <sup>b</sup>	0.406	1.100(20)	1.004(2)
X3 <sup>b</sup>	0.434	1.066(17)	1.002(2)
X4	0.474	1.000(18)	1.007(2)
X5	0.500	1.004(18)	1.009(2)
X6	0.616	1.000(20)	1.006(2)
X7	0.678	0.988(18)	1.007(2)
X8	0.715	1.003(17)	1.004(2)
X9	0.715	1.003(16)	1.004(2)
X10	0.739	0.978(19)	1.008(2)
N11	0.715	1.014(24)	1.011(7)

<sup>a</sup>Crystals were either studied by X-ray diffraction (X1–X10) or neutron diffraction (N11). The “melt” column specifies the Li charge content of the melt, [Li]/([Li]+2[Fe]). <sup>b</sup>Crystals with clear nonstoichiometry (X1–X3).

A comparison of crystals suggests that the majority of samples (X4–X10, N11) can be considered to be fully stoichiometric. Their Li sites are fully occupied within about one standard deviation. The Fe site occupancy refines to a value which is slightly higher (0.5–1.0%) than full occupancy, which is aphysical if taken at face value but which more likely reflects a slight aberration related to fixing the P occupancy to precisely one when its electrons are also involved in the covalent bonding that leads to nonspherical O ions. There is no evidence for antisite defects in these samples, which would show up as excess occupancy on the Li site and reduced occupancy on the Fe site. The statistical errors suggest an estimated standard deviation of about 0.2% in determining the Fe site occupancy and about 2.0% in determining the Li site occupancy, though the sensitivity to Fe on the Li site is much greater (also about 0.2%) since the Fe scattering power is about 10 times larger than that of Li. Site disorder was also addressed using neutron diffraction data, though only a single data set was available (grown from the same batch as X-ray crystals 9 and 10). Refinements carried out with the oxygen occupancies fixed to one gave the same values for the Li and Fe sites [1.001(23) and 1.009(4), respectively] as refinements that were carried out with freely varying oxygen occupancies. The neutron diffraction

data provides no evidence for measurable quantities of site defects or antisite defects in these stoichiometric crystals.

The remaining three samples appear (X1–X3) to have a statistically significant amount of Fe on the Li site, suggestive of a concentration of  $\text{Fe}_{\text{Li}}$  defects as high as 1%. The different nature of these samples is consistent with PXRD results, which finds an enlarged unit cell for these three samples that is up to 0.2% larger than the crystals judged to be stoichiometric. The Fe site occupancy does appear to be reduced in these three samples by about 0.5% relative to the remaining crystals, though the refined occupancy does not drop below one. It therefore cannot be directly concluded from the refinements of site occupancies if the defects are the antisite defects (previously judged to be the most stable from DFT calculations) or if they are sarcopside-like defects with formula  $\text{Li}_{1-2x}\text{Fe}_{1+x}\text{PO}_4$ , as has been postulated based on the results of solid state syntheses exploring the phase behavior near  $\text{LiFePO}_4$ . The fact that these defect-containing crystals have only been observed as the products for Fe-rich melts, however, strongly suggests that the sarcopside defect model is the correct one as only this hypothesis predicts the dividing line between defect-containing and stoichiometric crystal growth products, as can be clearly seen in Figure 4. It has been previously reported that samples with 5–7% of  $\text{Fe}_{\text{Li}}$  defects can be produced,<sup>7,28</sup> and it is anticipated that if crystals with the much higher levels of defect concentrations can be prepared, a clear distinction between the two competing defect models could be made directly from site occupancies determined in single crystal diffraction studies.

There is strong indirect evidence that the observed defects in  $\text{LiFePO}_4$  crystals (X1–X3) are sarcopside-like. The defects cause a large increase in the *a*- and *c*-lattice parameters of  $\text{LiFePO}_4$  but do not substantially affect the *b*-axis, exactly as would be expected for a solid solution between olivine  $\text{LiFePO}_4$  and sarcopside  $\text{Fe}_3(\text{PO}_4)_2 \equiv \text{Fe}_{1.5}\text{PO}_4$  whose lattice parameters determined from laboratory XRD data are given in Table 4. These changes are graphically illustrated in Figure 4, where the lattice parameter changes expected for the introduction of 2.0% sarcopside (expected value based on the single crystal refined occupancy of 1.0% Fe on the olivine Li site) are marked in solid lines extending to the olivine limit at the flux composition of 0.4546 expected from the phase diagram to correspond to a single-phase olivine sample. Furthermore, when the cell parameters (*a*, *c*, *V*) of all ground single crystals studied by powder diffraction are plotted on a common axis of sarcopside fraction (Figure 4, bottom panel), it can be seen that this single variable very effectively describes the observed changes in all the different cell parameters.

**Defect Distributions in  $\text{LiFePO}_4$  Crystals.** While both powder and single crystal diffraction experiments provide information about the average behavior of olivine samples, TEM experiments provide a complementary local probe of olivine defects. Thin sections were cut from single crystal samples using FIB lift-off techniques with the thin dimension normal to the olivine *b*-axis, allowing the columns of Li sites (red dots in Figure 5) to be directly visualized using HAADF (*Z*-contrast) imaging without interference from the Fe sites (blue dots, present as bright spots in the image). To judge the sensitivity of the method to Fe defects on Li sites, image simulations based on the multislice method were carried out as a function of the degree of exchange between the Fe and Li sites to quantitatively investigate the contrast variations of each atomic column in the HAADF images (Supporting Informa-

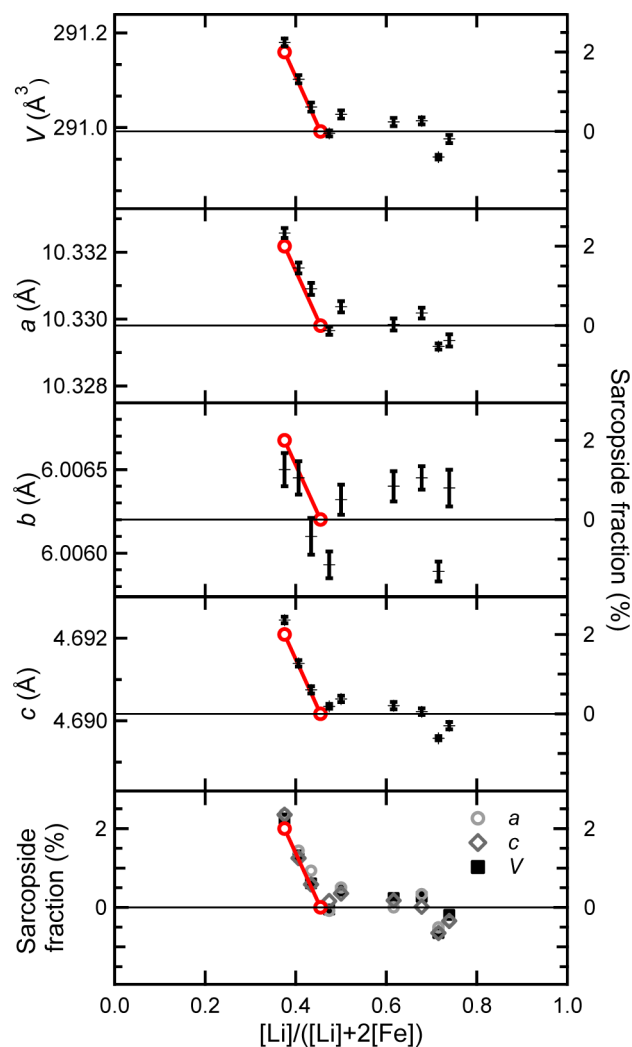


**Figure 4.** Top: Individual cell parameters (*a*, *b*, *c*, volume) of  $\text{LiFePO}_4$  crystals as a function of the Li content of the melt out of which they grew (left axis), and the fraction of sarcopside that this would correspond to if the lattice parameters vary linearly across a solid solution between olivine  $\text{LiFePO}_4$  and sarcopside  $\text{Fe}_{1.5}\text{PO}_4$  end members (right axis). The red line is drawn between two points: a 0% sarcopside at the point in the phase diagram corresponding to the onset of the  $\text{LiFePO}_4$ – $\text{Fe}_{1.5}\text{PO}_4$  solid solution ( $x = 0.4546$ ), and the extrapolated lattice parameters for the crystal grown from the most Fe-rich flux ( $x = 0.375$ ) at the Fe-content inferred from the single crystal structural refinement of this sample. Bottom panel: Overlay of the sarcopside fraction independently inferred from three cell parameters (*a*, *c*, *V*).

**Table 4.** Cell Parameters of Olivine and Sarcopside<sup>a</sup>

sample	olivine	sarcopside	$\Delta$
<i>a</i> (Å)	10.3298	10.4480	0.1182
<i>b</i> (Å)	6.0062	6.0299	0.0237
<i>c</i> (Å)	4.6902	4.7856	0.0954
$\gamma^\circ$	90	90.969	0.969
<i>V</i> (Å <sup>3</sup> )	290.99	301.45	10.46

<sup>a</sup>Comparison of the room temperature cell parameters of olivine  $\text{LiFePO}_4$  and sarcopside  $\text{Fe}_3(\text{PO}_4)_2$  measured on the same diffractometer. Sarcopside parameters are given in a nonstandard monoclinic setting ( $P112_1/a$ ) to facilitate comparison with olivine.

tion, Figure S6). Based on these simulations it is expected that lithium columns with 15% or more antisite defects can be

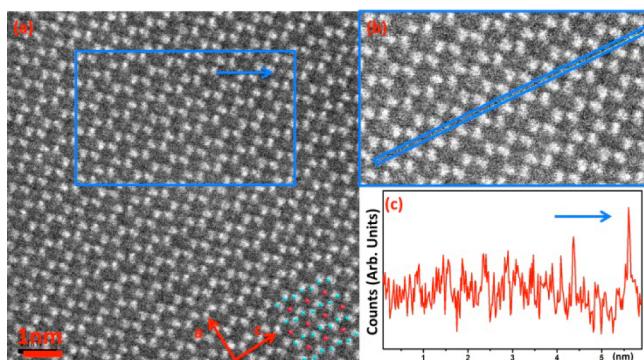


**Figure 5.** (a) Typical HAADF image of  $\text{LiFePO}_4$  in the  $[010]$  zone, allowing Li columns to be imaged. Atom columns for the Fe sites (blue dots) and Li sites (red dots) are marked in the lower right corner, while the arrow indicates a bright Li column containing  $\text{Fe}_{\text{Li}}$  defects. (b) Zoom of rectangular region in (a), indicating path of the line scan of image intensity shown in (c). Arrows in image and line scan mark the position of bright column with  $\text{Fe}_{\text{Li}}$  defects.

visualized as bright spots, while columns with fewer than 10% defects or no defects will be dark.

Further evidence of defect clustering was obtained in one single HAADF image, which showed an unusually high concentration of bright columns corresponding to 20% or more  $\text{Fe}_{\text{Li}}$  defects (Figure 6). In this area of this image, the high

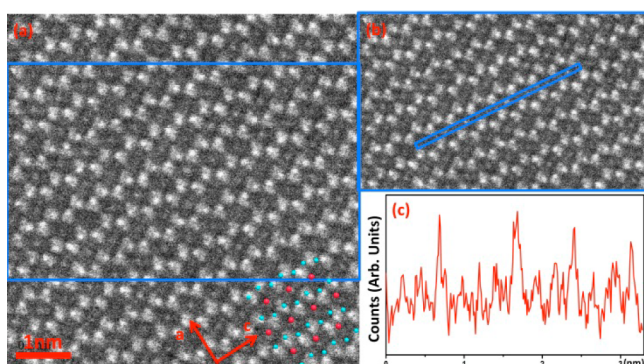


**Figure 6.** (a) Atypical HAADF image of  $\text{LiFePO}_4$  in the  $[010]$  zone with a very high concentration of bright Li columns. (b) Zoom of rectangular region in (a), indicating path of the line scan of image intensity shown in (c).

concentration of  $\text{Fe}_{\text{Li}}$  defects might plausibly be considered to belong to an endotaxial second phase rather than a simple isolated defect. Further work is necessary to definitively resolve whether or not highly defective regions of this type correspond to sarcopside or sarcopside-like intergrowths, though such intergrowths would provide a natural explanation for the observed clustering of  $\text{Fe}_{\text{Li}}$  defects. It is expected that  $\text{Fe}_{\text{Li}}$  defects will reduce ionic conductivity ( $\sigma_i$ ) by blocking ionic conduction channels while enhancing electronic conductivity ( $\sigma_e$ ) by creating bridges between the 1D Fe–O–Fe pathways for electronic conduction. Quantitative measurements of  $\sigma_i$  and  $\sigma_e$  in olivine single crystals as a function of crystallographic direction, defect concentration, and temperature are in progress.

## 4. CONCLUSIONS

It has been demonstrated that reciprocal salt flux growth methods using mixed  $\text{LiCl-FeCl}_2$  salts can be used to produce large stoichiometric  $\text{LiFePO}_4$  crystals which are either stoichiometric or which have low levels of  $\text{Fe}_{\text{Li}}$  defects within the Li-ion conducting channels based on the results of single crystal (X-ray and neutron) structure determinations. A sarcopside mechanism for defect formation ( $2 \text{Li}^+ \rightarrow \text{Fe}^{2+} + \text{vacancy}$ ) is supported by a variety of measurements, including refined stoichiometries, the systematic variation in lattice parameters, and the observed phase behavior. These results emphasize the existence of a thermodynamically stable solid solution in iron olivines with the  $(\text{Li}_{1-2x}\text{Fe}_x)\text{FePO}_4$  stoichiometry that is expected to form for any sample which is Fe-rich relative to the ideal  $\text{LiFePO}_4$  composition. Highly inhomogeneous concentrations of defects observed in TEM studies suggest that there may be endotaxial growths of sarcopside  $\text{Fe}_3(\text{PO}_4)_2$  within a host olivine lattice. Structural models of  $\text{LiFePO}_4$  obtained from single crystal X-ray diffraction and single crystal neutron diffraction have been compared and found to be nearly indistinguishable in atomic positions and in anisotropic displacement parameters, and represent the most definitive structural analysis to date for this system. While some classes of commercial  $\text{LiFePO}_4$  samples are prepared directly from the melt, flux-grown crystals have the advantages of lower preparation temperatures and a controllable defect composition that may facilitate the production of  $\text{LiFePO}_4$  electrodes with high tap densities.

## ■ ASSOCIATED CONTENT

### Supporting Information

Melting points for compounds in the  $\text{Li,Fe,Cl,PO}_4$  system, estimated melting relations, figure of a face indexed crystal, ORTEP-like figure of  $\text{LiFePO}_4$  unit cell, individual cell parameters for batches used in this study, tables detailing neutron and X-ray diffraction experiments and resulting crystallographic parameters, detailed X-ray refinement results for site occupancies, detailed analysis of extinction, MEM-based electron density maps, detailed TEM figures, variation of all crystallographic parameters as a function of growth conditions. This material is available free of charge via the Internet at <http://pubs.acs.org>.

## ■ AUTHOR INFORMATION

### Corresponding Author

\*E-mail: [kpete@bnl.gov](mailto:kpete@bnl.gov).

### Notes

The authors declare no competing financial interest.

## ■ ACKNOWLEDGMENTS

Research supported as part of the Northeastern Center for Chemical Energy Storage (NECCES), an Energy Frontier Research Center funded by the U.S. Department of Energy, Office of Basic Energy Sciences, under Award DE-SC0001294, including matching support from NYSTAR-NYSDED. Fruitful discussions with G. Ceder, R. Kostecki, M. S. Whittingham, C. P. Grey, their group members, and other members of NECCES are gratefully acknowledged. This research utilized the facilities at the Center for Functional Nanomaterials, Brookhaven National Laboratory, which is supported by the U.S. Department of Energy, Office of Basic Energy Sciences, under Contract No. DE-AC02-98CH10886. The TOPAZ experi-

ments at Oak Ridge National Laboratory's Spallation Neutron Source were sponsored by the Scientific User Facilities Division, Office of Basic Energy Sciences, U.S. Department of Energy. The STEM experiments were carried out at the ORNL Shared Research Equipment (SHaRE) User Facility, which is sponsored by the Office of Basic Energy Sciences, U.S. Department of Energy. Additional thanks go to D. Middlemiss for calculating structure factors, V. Petricek for help with JANA, and P. Fenter and T. Fister for measurements of rocking curves. The Stony Brook University single crystal diffractometer was obtained through the support of the National Science Foundation Grant CHE-0840483.

## REFERENCES

- (1) Adams, S. J. *Solid State Electrochem.* **2010**, *14*, 1787.
- (2) Morgan, D.; Van der Ven, A.; Ceder, G. *Electrochem. Solid-State Lett.* **2004**, *7*, A30.
- (3) Islam, M. S.; Driscoll, D. J.; Fisher, C. A. J.; Slater, P. R. *Chem. Mater.* **2005**, *17*, 5085.
- (4) Nishimura, S.-i.; Kobayashi, G.; Ohoyama, K.; Kanno, R.; Yashima, M.; Yamada, A. *Nat. Mater.* **2008**, *7*, 707.
- (5) Malik, R.; Burch, D.; Bazant, M.; Ceder, G. *Nano Lett.* **2010**, *10*, 4123.
- (6) Biendicho, J. J.; West, A. R. *Solid State Ionics* **2011**, *203*, 33.
- (7) Chen, J. J.; Vacchio, M. J.; Wang, S. J.; Chernova, N.; Zavalij, P. Y.; Whittingham, M. S. *Solid State Ionics* **2008**, *178*, 1676.
- (8) Chung, S.-Y.; Choi, S.-Y.; Yamamoto, T.; Ikuhara, Y. *Phys. Rev. Lett.* **2008**, *100*.
- (9) Amin, R.; Balaya, P.; Maier, J. *Electrochem. Solid-State Lett.* **2007**, *10*, A13.
- (10) Amin, R.; Maier, J.; Balaya, P.; Chen, D. P.; Lin, C. T. *Solid State Ionics* **2008**, *179*, 1683.
- (11) Li, J.; Yao, W.; Martin, S.; Vaknin, D. *Solid State Ionics* **2008**, *179*, 2016.
- (12) Yakubovich, O. V.; Simonov, M. A.; Belov, N. V. *Sov. Phys.-Dokl.* **1977**, *22*, 347.
- (13) Upreti, S.; Chernova, N. A.; Xiao, J.; Miller, J. K.; Yakubovich, O. V.; Cabana, J.; Grey, C. P.; Chevrier, V. L.; Ceder, G.; Musfeldt, J. L.; Whittingham, M. S. *Chem. Mater.* **2012**, *24*, 166.
- (14) Chen, D. P.; Maljuk, A.; Lin, C. T. *J. Cryst. Growth* **2005**, *284*, 86.
- (15) Weichert, K.; Sigle, W.; van Aken, P. A.; Jamnik, J.; Zhu, C.; Amin, R.; Acarturk, T.; Starke, U.; Maier, J. *J. Am. Chem. Soc.* **2012**, *134*, 2988.
- (16) Santoro, R. P.; Newnham, R. E. *Acta Crystallogr.* **1967**, *22*, 344.
- (17) Mercier, M.; Bauer, P.; Fouilleu, B. C. R. *Seances Acad. Sci., Ser. B* **1968**, *267*, 1345.
- (18) Liang, G.; Park, K.; Li, J.; Benson, R.; Vaknin, D.; Markert, J.; Croft, M. *Phys. Rev. B* **2008**, *77*.
- (19) Chen, J.; Graetz, J. *ACS Appl. Mater. Interfaces* **2011**, *3*, 1380.
- (20) Streltsov, V. A.; Belokoneva, E. L.; Tsirelson, V. G.; Hansen, N. K. *Acta Crystallogr., Sect. B: Struct. Sci.* **1993**, *49*, 147.
- (21) Petricek, V.; Dusek, M.; Palatinus, L. *JANA2006*; Institute of Physics: Praha, Czech Republic, 2006; <http://jana.fzu.cz/>.
- (22) Larson, A. C.; Von Dreele, R. B. *General Structure Analysis System (GSAS)*; Los Alamos National Laboratory Report LAUR 86-748; Los Alamos National Laboratory: Los Alamos, NM, 1994.
- (23) Zambonini, F.; Malossi, L. *Z. Kristallogr.* **1931**, *80*, 442.
- (24) Kanno, R.; Takeda, Y.; Mori, M.; Yamamoto, O. *Chem. Lett.* **1987**, 1465.
- (25) Mercier, M.; Gareyte, J. *Solid State Commun.* **1967**, *5*, 139.
- (26) Wang, L.; Zhou, F.; Meng, Y. S.; Ceder, G. *Phys. Rev. B* **2007**, *76*, 165435.
- (27) Chen, G.; Song, X.; Richardson, T. J. *Electrochem. Solid-State Lett.* **2006**, *9*, A295.
- (28) Axmann, P.; Stinner, C.; Wohlfahrt-Mehrens, M.; Mauger, A.; Gendron, F.; Julien, C. M. *Chem. Mater.* **2009**, *21*, 1636.
- (29) Jensen, K. M. Ø.; Christensen, M.; Gunnlaugsson, H. P.; Lock, N.; Bøjesen, E. D.; Proffen, T.; Iversen, B. B. *Chem. Mater.* **2013**, *25*, 2282.
- (30) Hoang, K.; Johannes, M. *Chem. Mater.* **2011**, *23*, 3003.
- (31) Hoffmann, C.; Wang, X. P.; Frost, M. *TOPAZ*, 2009; <http://neutrons.ornl.gov/topaz>.

## NOTE ADDED AFTER ASAP PUBLICATION

This paper was published ASAP on November 6, 2013. Corrections were made to Tables 1 and 2 and the caption of Figure 2. The revised version was reposted on November 8, 2013.